Appl. Phys. B 83, 587–594 (2006)
DOI: 10.1007/s00340-006-2192-3

Applied Physics B
Lasers and Optics

Y. FANG[1,✉]
Q. ZHOU[2]

The imaging properties of photonic crystal slabs with effective negative refraction indexes

[1] Department of Physics, Zhenjiang Watercraft College, Zhenjiang, 212003 P.R. China
[2] Department of Physics, Jiangsu University of Science and Technology, Zhenjiang, 212003 P.R. China

Received: 19 November 2005/
Revised version: 27 February 2006
Published online: 27 April 2006 •

ABSTRACT The imaging properties of photonic crystals (PCs) with effective negative refraction indexes are studied by the finite-difference time-domain (FDTD) method. The images resulting from a PC are the results of the interaction of multiple mechanisms. The superlens phenomena are restricted within some special conditions, such as low source frequency, excitation of surface mode and little effect of Bragg diffraction.

PACS 78.20.Ci; 41.20.Jb; 42.70. Qs

1 Introduction

Since the concept of the left-handed materials (LHMs) or negative refraction index materials (NRIMs) was first proposed by Russian physicist Veselago in 1968, there has been great interest in flat slab imaging by negative refraction [1–20], which can be realized in photonic crystal (PC) or LHM. For the PC, the equifrequency surface (EFS) of Bloch's modes can be properly designed so that the group velocity (directed to the EFS normal) of Bloch's mode excited by an incident wave points to a negative-refraction direction [2]. Many researchers [1–19] verified that a point source on one side of a PC slab could be imaged into a real point image on the opposite side. They also attempted to connect this phenomenon to the mechanism of superlensing. The superlensing effect can potentially overcome the diffraction limit inherent in conventional lenses. X. Wang et al. demonstrated unrestricted superlensing in a triangular two-dimensional PC [3]. X. Wang's another work indicated that surface modes excited on the surface of the PC lens facilitate restoration of evanescent waves and carry the subwavelength image information [4]. X. Zhang studied the effect of interface and disorder on the far-field image in a two-dimensional PC based flat lens [5]. Zhang's another work showed that the position relation of the point source and images in the PC lens imaging system strictly obeys the simple rules of geometric optics [6]. Like the above references, most of these works used a certain source frequency, i.e., a certain negative refraction index -1 or other values. There has been little work considering the effect of different values of negative refraction indexes on the imaging of PC lens up to now. For the physical mechanisms of the imaging of flat slab, it seems no debate attributing them to the negative refraction caused by double negative permittivity and permeability in LHMs; however, there still exist some different understandings about the superlensing behavior of PC based on the negative refraction, which were described in [9] and [10]. Recently, Z.Y. Li et al. [9] did their further studies on the all angle negative refraction in the flat slab PC predicted by [8], and concluded that the imaging properties of the PC slab were dominantly governed by the self-collimation effect and complex near-field wave scattering effect, rather than by the all-angle negative-refraction effect. After these works, S. He et al. pointed out that the self-collimation effect occurred at smaller incident angles, whereas the negative refraction effect occurred at relatively larger incident angles [11]. Therefore, there might be many factors contributed to the PC slab imaging, and which one of them plays the role is dependent on the configuration of the PC and optical source. In this paper, we will study the imaging properties of the PC slab with different values of negative refraction indexes and different configurations, and examine the dependence of the position, resolution of image and negative refraction index in detail. In addition, we also consider the effect of Bragg diffraction on the imaging properties of the PC.

✉ E-mail: fangyt432@sohu.com, fang_yt1965@sina.com

2 The photonic crystal and calculation of effective negative refraction index

For the point source imaging system, we select a triangular lattice of air holes in GaAs background with electric permittivity $\varepsilon = 12.96$. The hole radius is given $r = 0.4a$ and a is lattice constant. Only the transverse magnetic (TM) modes are considered here (the electric field is parallel to the axis of the air holes), thus the electromagnetic field of every point can be indicated by E_z, H_x and H_y. For general crystalline compounds, the optical loss is very small, and then we neglect it in our calculation. We obtain the photonic band structures for above PC using the standard plane expansion, which are shown in Fig. 1, in which the frequency is in unit of $2\pi c/a$ (c is the light velocity in vacuum). It is noticed that the second band near the gap becomes convex. Figure 2a gives the three-dimensional representation of band structure from $\omega = 0.25(2\pi c/a)$ to $\omega = 0.34(2\pi c/a)$ (for simplicity, the unit $2\pi c/a$ of frequency is omitted in the later), and Fig. 2b shows the corresponding EFS. The shape of EFS is almost circular for the higher frequencies, which means that the wave propagation is isotropic-like at these frequencies. For the isotropic frequency range, the effective refractive index concept can be

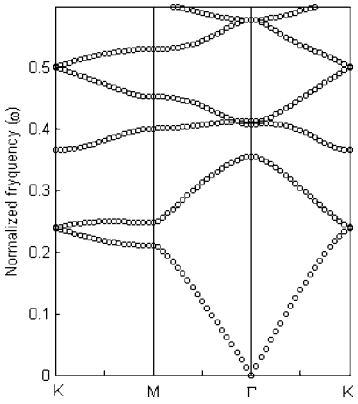

FIGURE 1 The band structure of 2D PC photonic crystal with triangular lattice of air holes

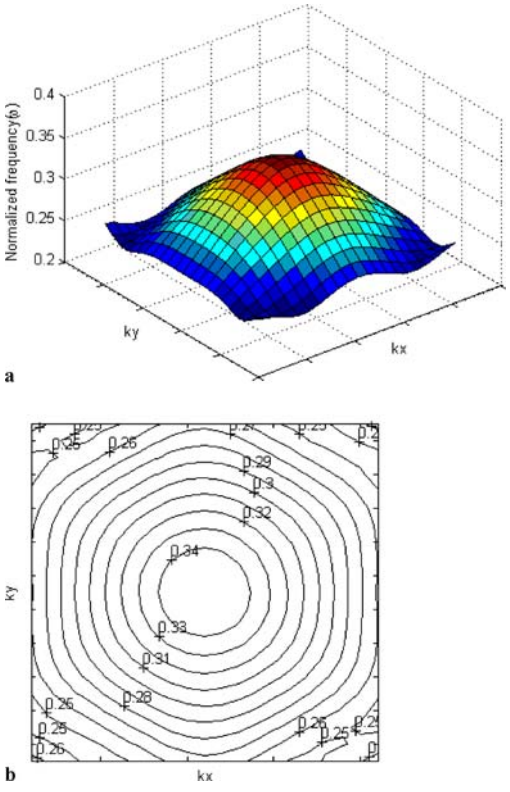

FIGURE 2 (**a**) The 3-D representation of the band structure. (**b**) The corresponding EFS for (**a**)

used for description of light propagation, and light refraction is simply described by Snell's law. Meanwhile, the direction of group velocity vector $\boldsymbol{v}_g = \nabla_k \omega$ is the direction of the energy flow, which is normal to the EFS. Since the group velocity for the second band is negative due to the all-convex shape of the EFS, the direction of waves is inward from the circular EFS. To clearly describe it, the schematic wave-vector diagrams are shown in Fig. 3 for the wave propagation with $\omega = 0.3$ from air to the PC. The blue arrows indicate two wave vectors from two different spaces, and the red arrow refers to the group velocity vector in the PC. Remember that the continuity of tangential components of the wave vector across the interface determines the $\boldsymbol{k}$ vector in the second material. Thus the effective negative refraction index for a certain frequency can be calculated by $n_{\text{eff}} = -\sin\alpha/\sin\beta = -r/r_0$, where r_0

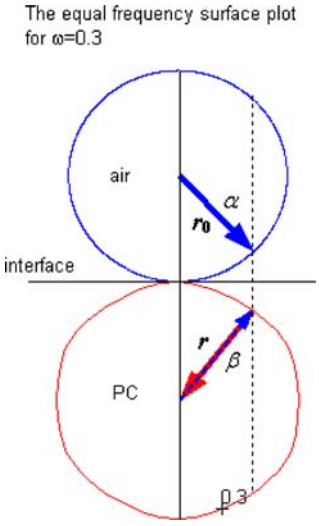

FIGURE 3 The schematic wave-vector diagrams are shown in Fig. 3 for the wave propagation from air to the photonic crystal

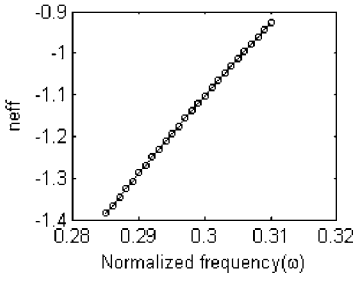

FIGURE 4 The calculated effective refraction index as a function of frequency in the second band of the PC

and r are the radius of two EFSs in air and the PC, respectively. The calculated results for frequencies (0.285–0.31) are shown in Fig. 4, from which we find the frequency with $n_{\text{eff}} = -1$ is 0.305.

3 The calculating model and method

In order to verify our above conjecture depicted by Fig. 1, we perform a numerical simulation based on the finite-difference time-domain (FDTD) method, which is a very powerful method to analyze electromagnetic problem due to its simplicity and accuracy. In a two-dimensional case, the electromagnetic fields can be decoupled into two transversely polarized modes, namely, the TE mode and the TM mode. For a linear isotropic material in a source-free region, the time-dependent Maxwell's equations can be discretized in space and time by a so-called Yee-cell technique [17, 18]. The following FDTD time stepping formulas are the spatial and time discretizations of Maxwell's equations on a discrete two-dimensional mesh within the x–y coordinate system for the TM mode,

$$H_x\Big|_{i,j+1/2}^{n+1/2} = H_x\Big|_{i,j+1/2}^{n-1/2} - \frac{\Delta t}{\mu_0}\frac{E_z\Big|_{i,j+1}^{n} - E_z\Big|_{i,j}^{n}}{\Delta y}, \tag{1}$$

$$H_y\Big|_{i+1/2,j}^{n+1/2} = H_y\Big|_{i+1/2,j}^{n-1/2} + \frac{\Delta t}{\mu_0}\frac{E_z\Big|_{i+1,j}^{n} - E_z\Big|_{i,j}^{n}}{\Delta x}, \tag{2}$$

$$E_z\Big|_{i,j}^{n+1} = E_z\Big|_{i,j}^{n} + \frac{\Delta t}{\varepsilon_{i,j}}\left(\frac{H_y\Big|_{i+1/2,j}^{n+1/2} - H_y\Big|_{i-1/2,j}^{n+1/2}}{\Delta x} - \frac{H_x\Big|_{i,j+1/2}^{n+1/2} - H_x\Big|_{i,j-1/2}^{n+1/2}}{\Delta y}\right), \tag{3}$$

where the index n denotes the discrete time step, indices i and j denote the discretized grid point in the x–y plane, respectively. Δt is the time increment, and Δx and Δy are the intervals between two neighboring grid points along the x and y directions, respectively. In our computation, $\Delta x = \Delta y = a/20$. The electromagnetic field inside the computation region is modeled by repeatedly applying (1)–(3); at each repetition, the whole field distribution is evaluated using the known distribution at the previous time step. In our computation, we set 324×524 cell numbers and $\Delta t = \frac{1}{2c\sqrt{(\Delta x)^{-2}+(\Delta y)^{-2}}}$ (c is light velocity) which can give a stable and convergent solution of the above equations. Similar equations for the TE mode can be easily obtained. Special consideration should be given at the boundary of the finite computational domain, where the fields are updated using special boundary conditions as information out of the domain is not available. Here, we use the perfectly matched layer (PML) method [18] for the boundary treatment.

The PC structure is given in Sect. 2. The sizes and positions of PC slabs in the computing space are given four kinds, which are shown in Fig. 5. All the sizes of PC slabs in the x direction are 300 (from 12 to 312), and in the y direction are as follows: 94 (from 160 to 254) for Fig. 5a, 111 (from 160 to 271) for Fig. 5b, 139 (from 132 to 271) for Fig. 5c and 147 (from 132 to 279) for Fig. 5d. For every PC structure, we select different termination. By the termination, we mean that we cut some part from the outside rows of air holes. All the lower and upper termination are as follows: $0.3a$ and $0.15a$ for Fig. 5a, $0.3a$ and $0.2a$ for Fig. 5b, $0.4a$ and $0.4a$ for Fig. 5c, and $0.4a$ and 0 for Fig. 5d. Then we give five computing models. Models One and Two are based on Fig. 5a, b, respectively, and give a point source at same position, i. e., at (162, 150). Model Three is based on Fig. 5c and gives a point source at (162, 122). Model Four is also based on Fig. 5c and gives a point source at (162, 112). Model Five is based on Fig. 5d and gives a point source at (162, 112). The distance between source and PC slab is $0.5a$ for the former three models, and a for the latter two models. For every model, we perform calculation by FDTD using source frequencies from 0.285 to 0.31 with an added step of 0.001, which correspond to effective negative refraction indexes from -1.385 to -0.926.

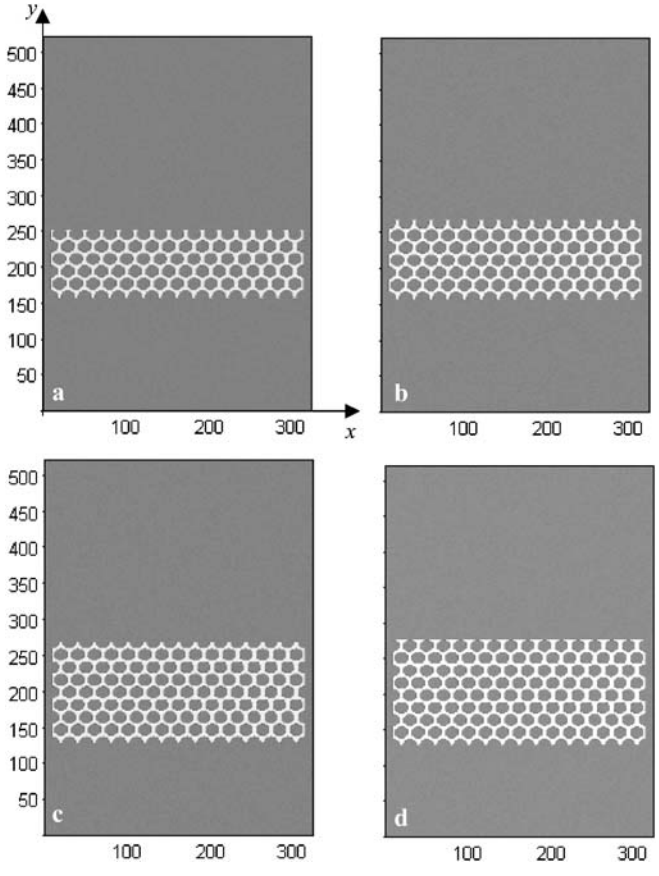

FIGURE 5 The four kinds of PC configurations in the computing space indicated by (**a**), (**b**), (**c**) and (**d**). The unit of axis is cell number. All the sizes of PCs in the x direction are 300 (from 12 to 312). The sizes of PCs in the y direction are as follow: 94 (from 160 to 254) for (**a**), 111 (from 160 to 271) for (**b**), 139 (from 132 to 271) for (**c**) and 147 (from 132 to 279) for (**d**)

4 The properties of images and negative refraction index

In this section, we give the detailed simulation results of the above five models. Figures 6–9 show the three-dimensional representation of electric field intensity for the Models One–Four at four frequencies: 0.285, 0.295, 0.305 and 0.310, which correspond to the effective negative refraction indexes of -1.385, -1.195, -1 and -0.926, respectively. Although light cannot focus at one point with $n_{\text{eff}} \neq -1$, the ray aberration is very small if n_{eff} is near to -1 and there is still a maximum value of electric field intensity at one point. We still call it as an imaging point in this paper. For simplicity, all the pictures include only the imaging space, i.e., they are drawn from the upper interface of the PC slab (see Fig. 5). For each model, the electric field intensities in z-axis are multiplied by same coefficient. From all the figures, we find that the imaging intensity, position and resolution are clearly dependent on the values of the effective negative refraction index and the PC configurations. For a definite model, the less absolute value of n_{eff}, the less the imaging intensity and the lower the imaging resolution. In order to further verify above rules, Fig. 10a and b plot the average electric field intensity distribution along two lines in the vertical and horizontal directions, respectively, which are all through the centers of the images. Figure 10c depicts the full width half maximum (FWHM) of the images obtained from the vertical and horizontal direction. Clearly, the resolution of image in horizontal direction is much higher than that in the vertical direction. Furthermore, the FWHM of the images in the horizontal direction is much less than the wavelength and rarely changes with n_{eff}. However, the FWHM of the images in the vertical direction is larger than the wavelength after $n_{\text{eff}} > -1.2$ and increases quickly with n_{eff}. Although the above results are obtained

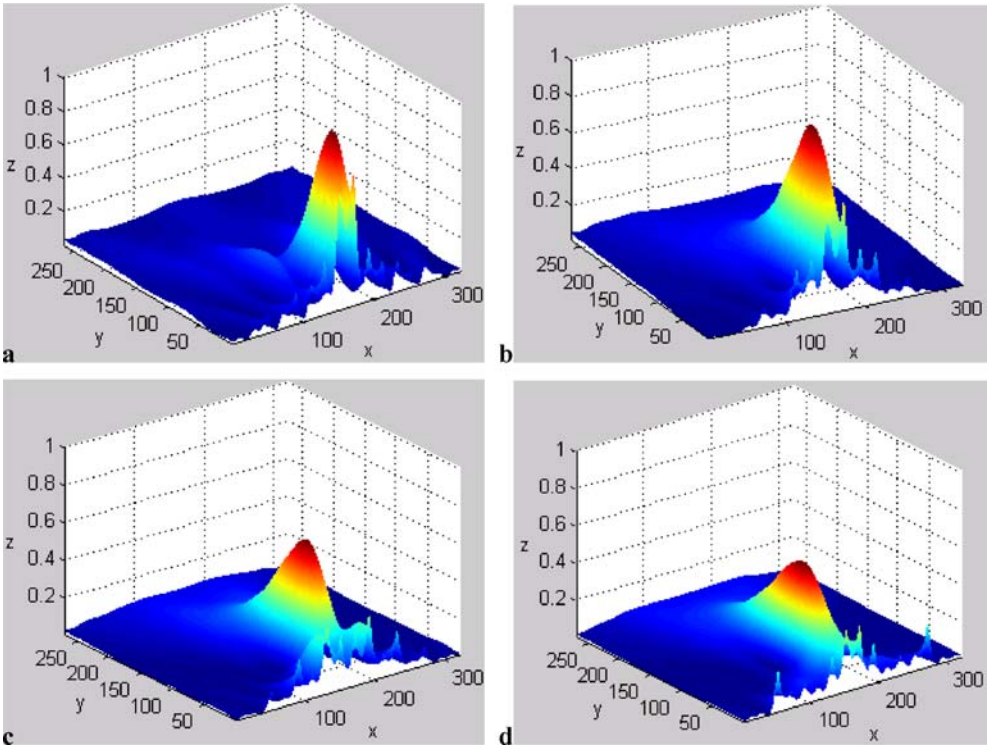

FIGURE 6 The 3-D representation of electric field intensity at four frequencies: 0.285, 0.295, 0.305, 0.310 for Model One

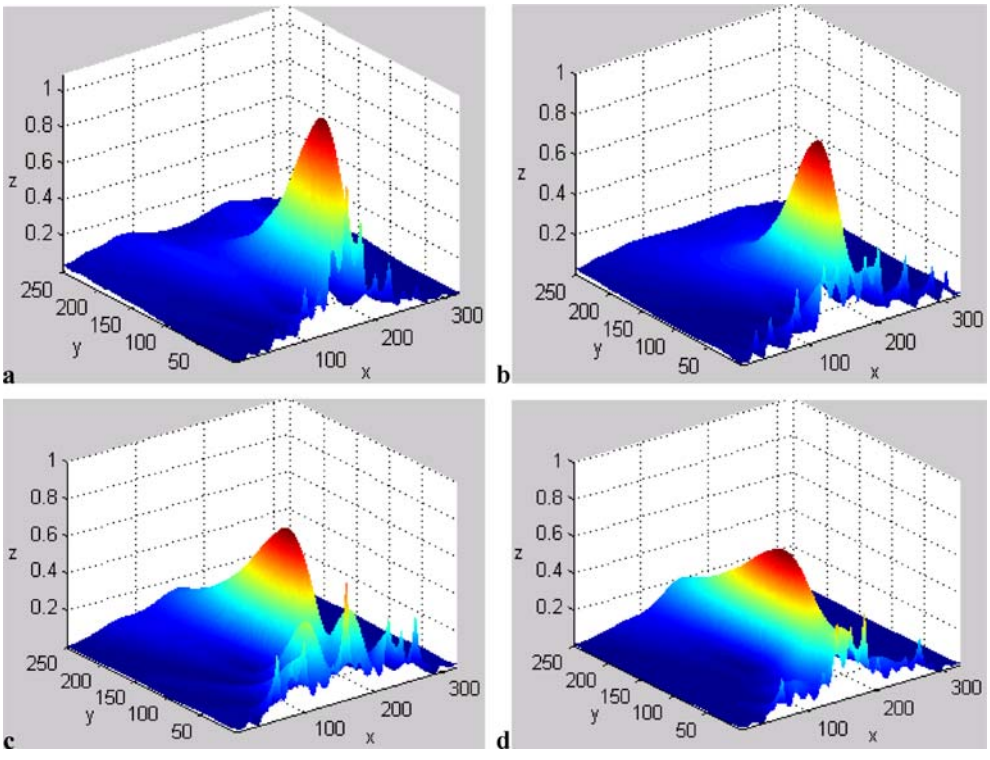

FIGURE 7 The 3-D representation of electric field intensity at four frequencies: 0.285, 0.295, 0.305, 0.310 for Model Two

mainly from Model One, our calculations for other models obtain similar results. All these results show that superlens phenomena are restricted in the low frequency domain. There must be other mechanisms limiting the superlens behavior, which will be discussed in later parts.

We also consider the effect of the PC configuration on the imaging properties. Given the same frequency $\omega = 0.305$ which corresponds to $n_{\text{eff}} = -1$, Fig. 11 plots the average electric field intensity distribution along two lines through the centers of the images in the vertical and horizontal directions as Fig. 10 does. It is clear that the resolution and intensity of images decrease with the thickness of the PC slab increasing. But there is an exception that the resolution and the intensity of images for Model One is similar to those for Model Two, though the thickness of the PC slab in Model Two is larger than that in Model One. This can be attributed to the excitation

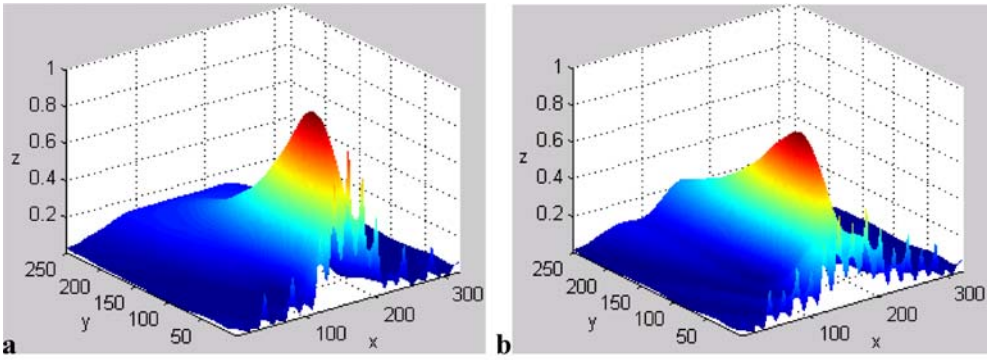

FIGURE 8 The 3-D representation of electric field intensity at four frequencies: 0.285, 0.295, 0.305, 0.310 for Model Three

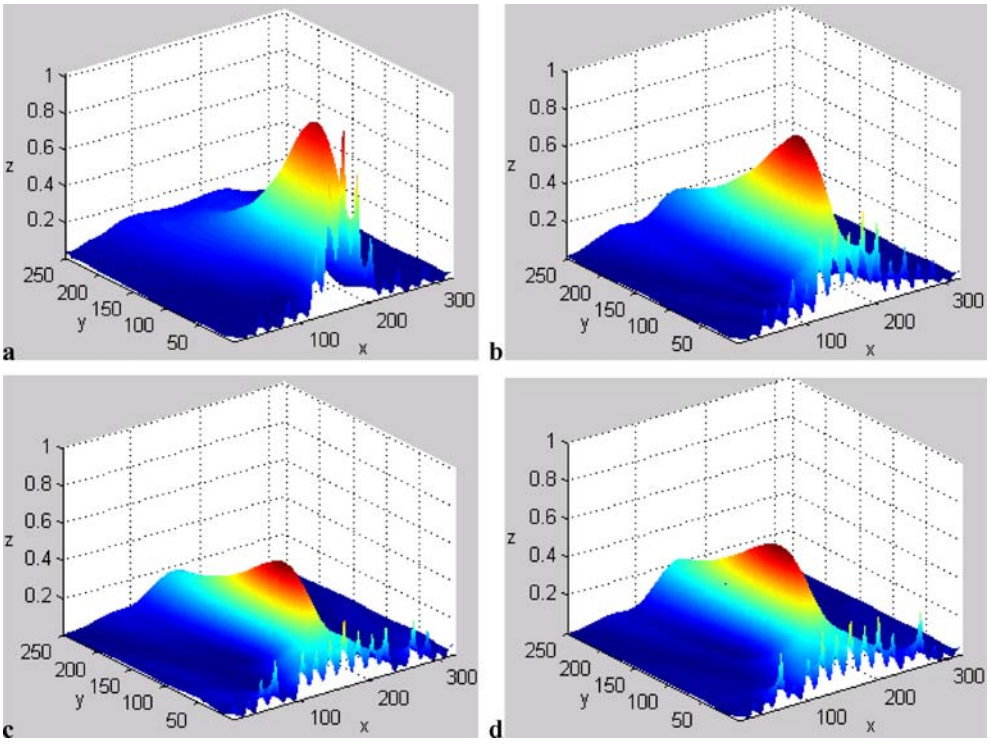

FIGURE 9 The 3-D representation of electric field intensity at four frequencies: 0.285, 0.295, 0.305, 0.310 for Model Four

of the surface mode at the interface due to proper termination. References [4], [7] and [11] told us that the surface mode can facilitate restoration of the evanescent waves, which carries the subwavelength image information. From Figs. 7c and 11a, we find the field intensity at the upper interface of the PC slab for Model Two is much larger than that for other models.

Next, we study the relation of the image position and negative refraction index. According to Sect. 2, if PC has the effective negative refraction index, the light propagation in the PC obeys the rules of geometric optics. Thus we can easily evaluate the image point position by Snell's law. For the case of $n_{\text{eff}} \neq -1$, the image point position is obtained approximately. Because the point source is at the perpendicular bisector of the PC slab, i.e., $x = 162$, the image point position can be decided only by the y coordinate. By Snell's law, we calculate all the coordinates of image points from Model One to Model Four. On the other hand, we measure all the coordinates of image points by FDTD, from which the position

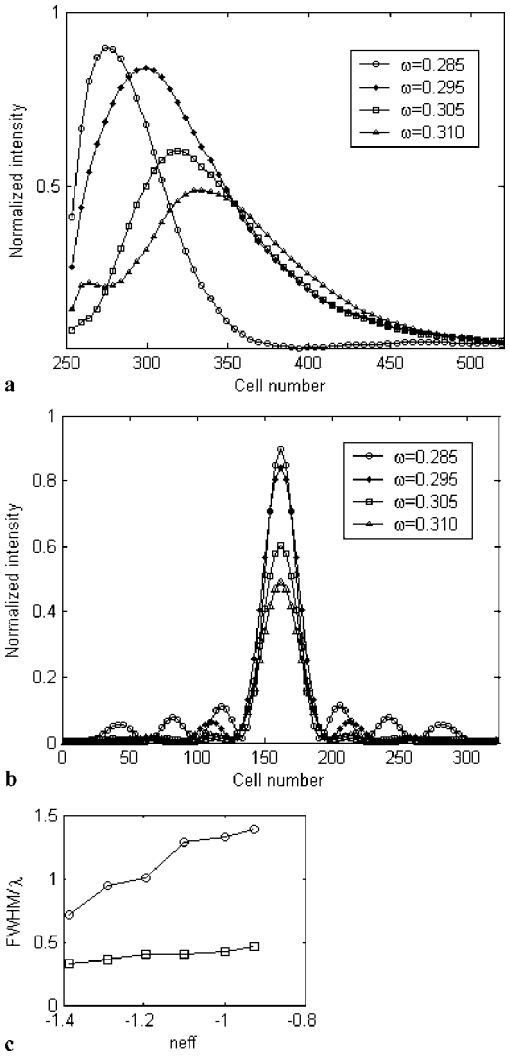

FIGURE 10 (**a**) The average electric field intensity distribution for Model One along the vertical line across the center of the image (i.e., $x = 162$, see Fig. 5a). Every curve begins from the upper interface of each slab. (**b**) The average electric field intensity distribution for Model One on the horizontal lines $y = 275, 300, 319, 332$ through the centers of the images (i.e., the maximums in Fig. 10a), respectively. (**c**) FWHM of images obtained from the vertical and horizontal directions for different n_{eff}. The *circle* points are from vertical direction and the *square* point from horizontal direction

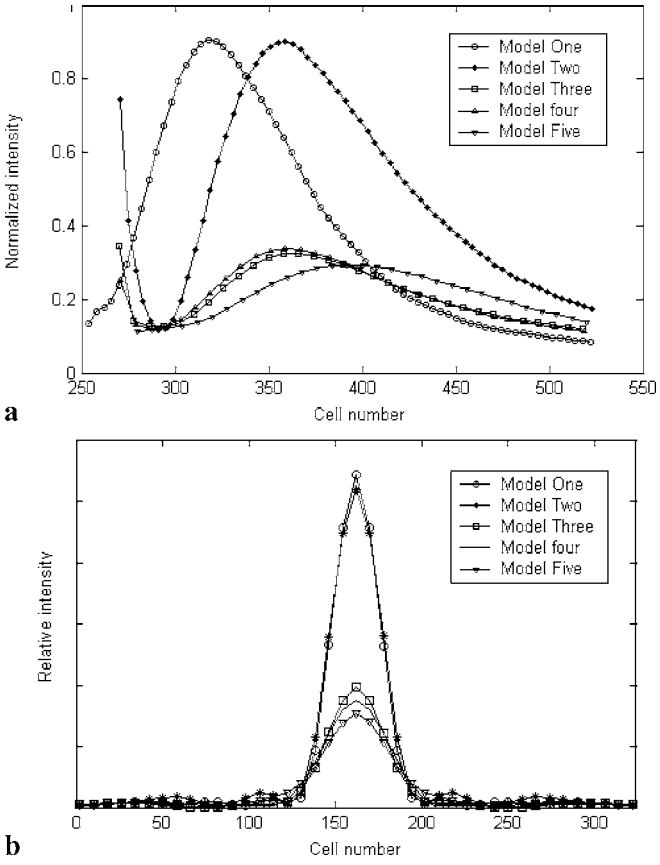

FIGURE 11 (**a**) The average electric field intensity distribution for different models along the vertical line across the center of the image (i.e., $x = 162$, see Fig. 5a) with same source frequency $\omega = 0.305$. Every curve begins from the upper interface of each slab. (**b**) The average electric field intensity distribution along the horizontal lines across the centers of the images for different models

of image point is decided by the maximum value of average field intensity along $x = 162$. The results of two methods are shown in Fig. 12. For all models, the y coordinates of the image points increase almost linearly with the n_{eff} by the Snell's law, but they are all dropped by FDTD. The decreasing of the y coordinates of the image points can be attributed to the self-collimation effect existing in the PC that moves the images inside the PC forward and the images outside the PC back. In addition, for the results of FDTD, the curves of the y coordinates of image points go up with n_{eff} generally, which is consistent with the results calculated by Snell's law, but there are some exceptions, for example, near $n_{\text{eff}} = -1.15$ in Fig. 12a and $n_{\text{eff}} = -1.3$ in Fig. 12b, they go down when n_{eff} increases. It should be noted that the curves of the y coordinates of image points by FDTD look like stairs in Fig. 12c and 12d, i.e., in some domains the y coordinates keep constant in spite of the change of n_{eff}. The abnormal phenomena have not been reported in recent published papers. Here we contribute them to Bragg diffraction effect of the PC, which we will discuss in next part.

5 Discussion and analysis

In Sect. 4, we conclude that the imaging resolution is dependent on the value of n_{eff} and the configuration of the PC, and the superlens phenomena are restricted within low frequency domain. Furthermore the position relations of the source and images do not strictly obey the Snell's law. All these show that the superlens phenomena of the PC are ideal models. The basis of the superlens phenomena of the PC is that we suppose the PC, an artificial inhomogeneous media, as homogeneous media. However, it is only suitable for light with low frequencies, because the lattice constants are much less than the wavelengths. For light with high frequencies, the Bragg diffraction effect in the PC cannot be omitted, because the lattice constants are near to the wavelengths in these case. The Bragg diffraction effect will result in many diffraction spots in the imaging space of the PC, just as the x light propagates through the crystal. In fact, the negative refraction effect and Bragg diffraction effect together exist inside the PC, and we think that the total result is the modulation of the negative refraction effect on Bragg diffraction effect. Of

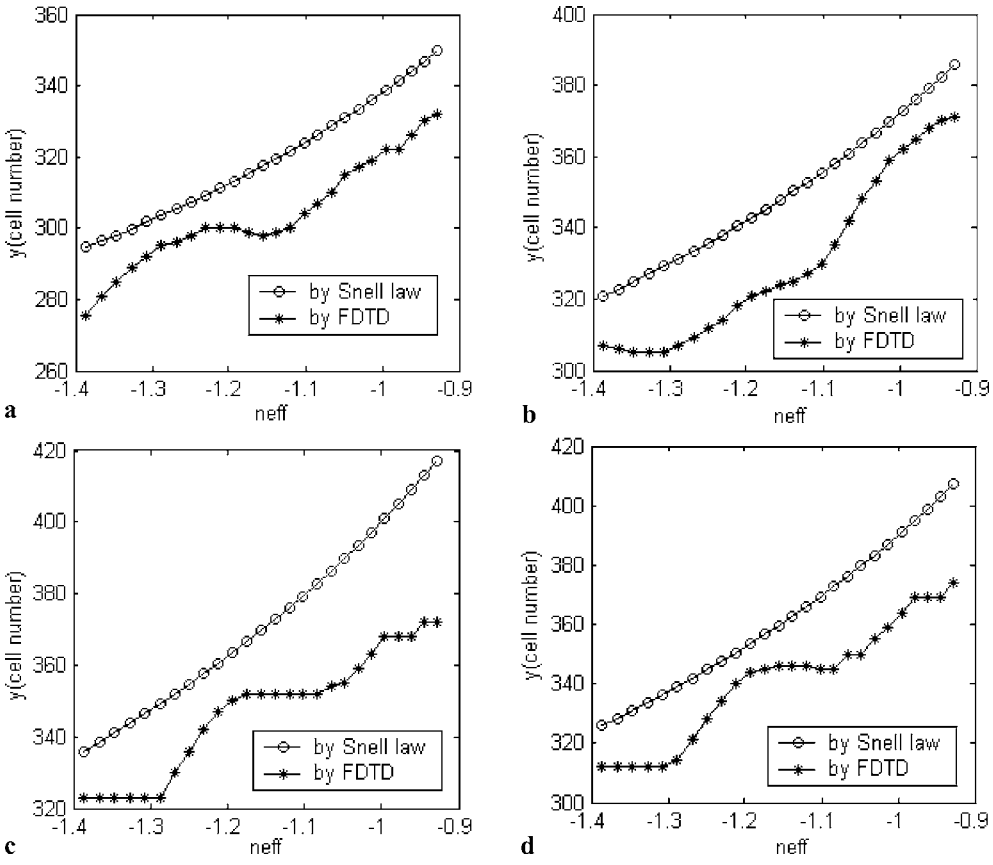

FIGURE 12 The coordination of images obtained by Snell's law and FDTD for Model One (**a**), Model Two (**b**), Model Three (**c**) and Model Four (**d**)

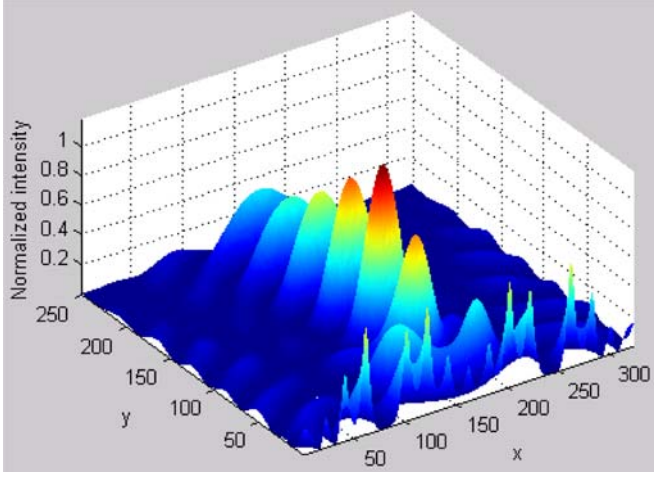

FIGURE 13 The distribution of instantaneous electric field intensity of imaging space with $\omega = 0.305$ for Model Four

course, there may be other factors such as self-collimation, surface mode and the losses of materials etc., which are all contributed to the imaging properties. It should be noted that we have ignored the effect of material losses. If we consider it, the image quality will become worse [20]. In order to observe the Bragg diffraction effect, we plot the distribution of instantaneous field intensity of imaging space with $\omega = 0.305$ for Model Four in Fig. 13. It is clear that besides a main peak on the optical axis, there are a series of smaller peaks lining up on this line and some much smaller peaks distributing on both sides of this line. All these smaller peaks can be regarded as the result of the Bragg diffraction. Because the diffraction peaks on the optical axis are much larger than the side peaks, the effect of the Bragg diffraction on the resolution of images along the vertical direction is much larger than that along the horizontal direction. This can explain why the resolution of images along the vertical direction is lower than those along the horizontal direction for all models. As for the y coordinate curves drops in Fig. 12a and b, and the y coordinate curves have stairs structure in Fig. 12c and d, we think that, for some source frequencies the effect of the Bragg diffraction has an advantage over that of negative refraction and the position of the peak value is decided by the Bragg diffraction. With a little change of source frequency or the value of n_{eff}, the diffraction peaks hold still or even fall back, which is dependent on the diffraction condition. In addition, the less the source frequency, the less effect of Bragg diffraction on the resolution of images. This also explains that when the frequency increases or the absolute value of n_{eff} decreases, the resolution of images becomes lower and lower (see Fig. 10). In fact, the effect of the Bragg diffraction on the images also appeared in other papers [3, 4]. Around the images, there were other clear optical spots (Fig. 4 in [3] and Fig. 2a in [4]), which were not explained in these papers.

6 Conclusions

In conclusion, we systematically study the imaging properties of the PC with different values of effective negative refraction index and different configurations. There are multiple mechanisms in the PC that are all attributed to

the imaging properties, including the Bragg diffraction, the excitation of surface mode and self-collimation. The Bragg diffraction occurs in high frequency domain and mainly influences the quality and position of image in the optical axis direction. The excitation of surface mode helps to improve the resolution of image, and the self-collimation make the position of the image deviate from the rules of geometric optics. It is hoped that our studies will be helpful for further understand the imaging properties of the PC with negative refraction.

ACKNOWLEDGEMENTS Supported by the National Natural Science Foundation of China under Grant No. 10574058.

REFERENCES

1 V.G. Veselago, Sov. Phys. Uspekhi **10**, 509 (1968)
2 M. Notomi, Phys. Rev. B **62**, 10 696 (2000)
3 X. Wang, Z.F. Ren, K. Kempa, Opt. Express **12**, 2919 (2004)
4 X. Wang, K. Kempa, Phys. Rev. B **71**, 233 101 (2005)
5 X. Zhang, Phys. Rev. B **71**, 165 116 (2005)
6 X. Zhang, Phys. Rev. B **70**, 195 110 (2004)
7 R. Moussa, S. Foteinopoulou, L. Zhang, G. Tuttle, K. Guven, E. Ozbay, C.M. Soukoulis, Phys. Rev. B **71**, 085 106 (2005)
8 C. Luo, S.G. Johnson, J.D. Joannopoulos, J.B. Pendry, Phys. Rev. B **68**, 045 115 (2003)
9 Z.Y. Li, L.L. Lin, Phys. Rev. B **68**, 245 110 (2003)
10 H.T. Chien, H.T. Tang, C.H. Kuo, C.C. Chen, Z. Ye, Phys. Rev. B **70**, 113 101 (2004)
11 S. He, Z. Ruan, L. Chen, J. Shen, Phys. Rev. B **70**, 115 113 (2004)
12 R.A. Shelby, D.R. Smith, S. Schultz, Science **292**, 77 (2001)
13 S. Foteinopoulou, C.M. Soukoulis, Phys. Rev. B **67**, 235 107 (2003)
14 E. Cubukcu, K. Aydin, E. Ozbay, S. Foteinopoulou, C.M. Soukoulis, Nature (London) **423**, 604 (2003)
15 P.V. Parimi, W.T. Lu, P. Vodo, S. Shridar, Nature **426**, 404 (2003)
16 Z. Ruan, M. Qiu, S. Xiao, S. He, L. Thylén, Phys. Rev. B **71**, 045 111 (2005)
17 Y. Fang, H. Sun, T. Shen, Opt. Mater., in press, corrected proof, available online 19, September 2005
18 Y. Fang, H. Sun, Chin. Phys. Lett. **22**, 2674 (2005)
19 A. Husakou, J. Herrmann, Opt. Express **12**, 6491 (2004)
20 X. Zhang, Phys. Rev. B **70**, 205 102 (2004)